Influence of Particle Geometry on Dispersion Forces

Yifei Liu,[1,2] Heping Xie,[1,2] Cunbao Li,[1,2,*] Dong-Sheng Jeng,[3,4] and Bo Nan Zhang[5]

[1] *Guangdong Provincial Key Laboratory of Deep Earth Sciences and Geothermal Energy Exploitation and Utilization, College of Civil and Transportation Engineering, Shenzhen University, Shenzhen 518060, China*

[2] *Shenzhen Key Laboratory of Deep Underground Engineering Sciences and Green Energy, Shenzhen University, Shenzhen 518060, China*

[3] *School of Engineering and Built Environment, Griffith University Gold Coast Campus, Queensland 4222, Australia*

[4] *College of Civil Engineering, Qingdao University of Technology, Qingdao 266033, China*

[5] *School of Nuclear Science and Technology, Lanzhou University, Lanzhou 730000, China*

(Received 20 October 2022; revised 31 January 2023; accepted 14 March 2023; published 6 April 2023)

Dispersion forces (van der Waals force and Casimir force) originating from quantum fluctuations are crucial in the cohesion of microscale and nanoscale particles. The nonadditivity of these forces and the complex geometry of realistic particles make conventional additive algorithms produce unacceptable errors, and it is experimentally challenging to identify the contribution of dispersion forces from the many forces that constitute the cohesion. In this study, we use the fluctuating surface current technique, an exact scattering theory-based nonadditive algorithm, to accurately quantify the influence of geometry on dispersion forces. To characterize the complex geometries, we employ a data-adaptive spatial filtering method and three-level descriptors. Our results determine the influence of multiscale surface fluctuations on dispersion forces. Additionally, we establish a convenient formula for predicting the dispersion forces between realistic particles with complex shapes from the exact Lifshitz solution via multistage corrections.

DOI: 10.1103/PhysRevApplied.19.044019

I. INTRODUCTION

Cohesion plays a key role in determining the behaviors of particles and particle systems ranging from the nanoscale to the microscale. The dispersion force is one of the main sources of cohesion. In nearly dry and uncharged particle systems with particle sizes less than 10 μm, dispersion forces dominate [1–4].

In different historical stages, the dispersion force has had various names. The earliest phenomenological name of the dispersion force was the "van der Waals force" [5], followed by the "London force" [6] and "Casimir force" [7]. However, in the 1950s, Lifshitz realized that these forces all originated from quantum fluctuations, and a unified theory was developed [8]. This theory can be applied to reproduce the van der Waals force (vdW force) and Casimir force as limiting cases of small and large separations. In this study, we use the general term "dispersion force" to refer to these forces with the same origin [9,10]. In reality, almost all particles have various irregular shapes that differ considerably from any idealized geometry, including both natural and artificial particles. Moreover, it has been proven both theoretically and experimentally that dispersion forces depend strongly on geometry, and changes in dispersion forces caused by geometric changes can reach several orders of magnitude. [11–13]. Therefore, it is of significance to quantify the influence of particle geometries on dispersion forces.

For objects with arbitrary shapes, including objects made from idealized materials, the dispersion force is challenging to calculate analytically [14]. At present, the most effective methods for determining the influence of geometry on the dispersion force are physical experiments and numerical calculations. Different experimental approaches have been developed in fields where these forces play important roles. Many experimental studies are based on two main types of measuring equipment: the surface force apparatus (SFA) and atomic force microscope (AFM). The SFA technique was developed by Israelachvili [15] and can be applied to measure the force between two macroscopically curved surfaces over relatively large areas with angstrom resolution. Some researchers have studied the effect of surface roughness on contact mechanics with SFA approaches [16,17]. However, because the measurements are generally carried out under loading conditions, it is difficult to extract the contribution of dispersion force from the various forces that make up the surface force.

AFM can accurately measure the interaction force between two microparticles [18]. Mohideen and Roy [19]

*cunbao.li@szu.edu.cn

precisely measured the dispersion force between a metal sphere and plate with AFM. An accurate measurement involves strictly excluding the contributions of forces other than the dispersion force, which is typically very difficult [12]. Therefore, at present, accurate measurements are limited to a few special geometries (sphere and plate) [20,21]. Although some studies have investigated particles with complex morphologies [22,23] with AFM, the environment was not strictly controlled, and the adhesion or cohesion was measured instead of the dispersion force. In addition, in the field of chemical engineering, the centrifugal method has been used to study the effects of particle morphology on cohesion and adhesion [24,25]. However, the centrifugal method is a rougher technique than SFA and AFM. Additionally, cohesion and adhesion were measured in this study as opposed to the dispersion force. Recently, in microelectromechanical systems, special equipment has been developed to quantify the effect of the boundary geometry on the dispersion force [13,26–29]. However, the research objects in these studies were artificial plates with relatively regular surfaces (rectangular silicon gratings and corrugated plates) rather than real particles with complex morphologies. Thus, in summary, previous experimental studies mainly focused on how particle geometry influences adhesion or cohesion and did not precisely determine the effect of the dispersion force. Critical experiments on the dispersion force are limited to a few special geometries and materials. Therefore, a general law about the influence of geometry on the dispersion force has not yet been established due to the lack of experimental data on real particles with complex morphologies.

Other effective methods include numerical calculations. Thus far, two approximate algorithms have been commonly applied because of their simplicity: pairwise summation (PWS) approximation and proximity force approximation (PFA) [30–32]. The PWS approximation, which is also known as the Hamaker summation [33], calculates the dispersion force between two macroscopic bodies according to the pairwise summation of volumetric elements interacting through the vdW-Casimir force, which can be established based on dipolar dispersive interactions. PFA, which is also known as the Derjaguin approximation, models the interaction between nearby surfaces as additive line-of-sight interactions between infinitesimal, planar surface elements (computed via the Lifshitz formula [34]). Both algorithms are based on the assumption of additivity, with the force calculated by simply summing the force contributions of the surface or dipole interactions. Unfortunately, a concise and convenient assumption always comes at the expense of accuracy. In fact, the interaction between two dipoles (surfaces) is influenced by nearby dipoles (surfaces), which is ignored in the additivity assumption. Moreover, the multiple scattering caused by multibody interactions cannot be ignored for condensed matter. The discrepancy between additive approximations and exact calculations is often referred to as nonadditivity. A detailed explanation of nonadditivity can be found in the review by Rodriguez *et al.* [12]. Nonadditivity considerably reduces the accuracy of PWS and PFA techniques for handling condensed matter with complex morphology, which has been confirmed by several theoretical and experimental studies [11,13,35–37]. Therefore, these two additivity methods cannot be applied to study the influence of geometry on the dispersion forces of real particles.

Obviously, the interactions among each dipole are impossible to calculate except at the subnanometer scale [37,38]. As previously mentioned, dispersion forces originate from quantum fluctuations. In terms of field fluctuations, the issues caused by nonadditivity can be addressed. This kind of algorithm originated in the 1950s [34] and was designed to work for one special geometry. Since 2007 [39], dramatic progress has been made in this field, and general-purpose schemes for arbitrary materials and various geometric configurations have been developed [40]. These schemes can be roughly divided into two categories according to the choice of physical basis: fully quantum mechanical approaches and semiclassical approaches. The former include the path integral (or scattering) approach [39,41] and the lattice field approach [14,42], which are highly efficient in certain geometries but not flexible enough for general geometries, especially geometries with sharp corners [40]. In the semiclassical approach (also known as the stress tensor approach) [43,44], the computation of the fluctuation force can be reduced to solving the classical electromagnetic scattering problem according to the fluctuation-dissipation theorem. Thus, many classical electrodynamics methods can be applied after a few important modifications (detailed in the reviews of Rodriguez *et al.* [12] and Johnson [45]). In addition to these two schemes, the fluctuating surface current (FSC) technique (which will be introduced in detail in Sec. II B) developed by Reid *et al.* [46] can be regarded as a third scheme that combines the advantages of the previous two approaches. In these nonadditivity algorithms, interactions among instantaneous dipoles are not considered and are replaced by the global optical response of the material, which can be described by macroscopic dielectric functions. Based on the dielectric functions of the materials, the dispersion force can be accurately calculated by considering the complex electromagnetic modes and surface scattering properties [30]. The accuracy of these algorithms has been confirmed by strict experiments, even in cases with complex geometric configurations [13,26,40]. As Svetovoy and Palasantzas [10] noted, these nonadditivity algorithms should be the most suitable numerical methods for studying the influence of particle geometry on dispersion forces. The generality of these methods does, however, come at a price, with even the most sophisticated

of formulations requiring thousands or hundreds of thousands of scattering calculations to be performed. Moreover, the calculation accuracy needs to be guaranteed by obtaining accurate dielectric functions for the materials, which are usually empirical. Therefore, at present, these algorithms are still limited to a small number of special materials and geometries, and few related calculations have been reported for real particles with complex morphologies.

In summary, no general law about the influence of particle geometry on dispersion forces has been established. Most previous experimental studies focused on surface or cohesion forces instead of the dispersion force, which requires that the experimental environment be strictly controlled, and critical experimental studies were limited to a few special geometries and materials. Moreover, the conventional calculation methods are based on the assumption of additivity, which is not suitable for real particles with complex morphologies. Recent nonadditivity algorithms were developed based on field fluctuations and can be applied to accurately calculate dispersion forces in complex geometric configurations; however, these techniques are also limited to a small number of geometries and materials. In this research, we apply a form of this exact technique to perform large-scale brute-force computations to develop a general law on how particle geometry influences dispersion forces. The remainder of this paper is organized as follows. First, we introduce a reasonable characterization of complex morphologies based on spherical empirical modal decomposition, including a multiscale decomposition of the morphology and a three-level characterization of real particles. Then, an accurate numerical model for determining the dispersion force beyond nonadditivity, namely, the FSC algorithm, is briefly introduced. Then, the dispersion forces of particles with different morphologies are calculated. We produce different geometric configurations for the same morphology through random rotations. According to the calculation results, we present a general law on the influence of multiscale surface fluctuations on the dispersion force. Furthermore, through multistage approximations, we propose a convenient formula for predicting the dispersion force between real complex shaped particles that can be used in engineering applications.

II. METHODS

A. Characterization of particle geometry

As previously mentioned, real microparticles (which are encountered in daily life, such as pollen, sand, dust, and flour) have a variety of irregular shapes that differ substantially from any idealized geometry, regardless of whether the particles are natural or artificial. Ideal geometries such as spheres and cubes can be fully characterized by simple parameters such as the radius, edge length, area, and volume. However, these simple parameters cannot be applied to characterize the geometrical properties of complex irregular particles. In fact, despite almost a century of discussion, a reasonable characterization of irregular geometries has not yet been established [47,48].

There is a consensus that irregular geometries are too complex to be characterized by a single parameter at one scale [49,50]. The existing particle morphology characterization methods can be roughly divided into two categories: Euclidean descriptors and frequency domain descriptors. The Euclidean descriptor is a traditional descriptor that extracts description parameters by combining basic parameters such as the axial length, volume, surface area, and local curvature of the particles. Dozens of Euclidean descriptors have been proposed since the first was established by Wadell [51]. The frequency domain descriptor is a recent descriptor [52,53] that decomposes the morphology into a combination of orthogonal functions by appropriate function transformations [commonly, Fourier transforms for two-dimensional (2D) morphologies and spherical harmonic transforms for 3D morphologies] and extracts different order coefficients of the transformation functions to characterize particles at different scales. These descriptors reflect the multiscale characteristics of the morphology.

Since the two types of descriptors provide different views on morphological characterization, we employ slightly modified versions of both descriptors in this study. Here, instead of the frequency domain descriptors themselves, we consider the decomposition (function transformation) process in this study, which decomposes the complex morphologies of real particles into surface fluctuations at different scales. The commonly used Fourier transform and spherical harmonic transform are suitable only for stationary signals because they are global transformations in the time domain, while the morphologies of real particles are typically nonstationary signals (with nonstationary characteristics such as sharp corners, planes, edges, and other abrupt features). Therefore, in the decomposition process, we introduce the spherical empirical mode decomposition (SEMD) technique [54,55], the core algorithm of the Hilbert-Huang transform [56], which works well for nonstationary signals. The physical essence of SEMD is a data-adaptive spatial filter. As shown in Fig. 1(a), taking the average of the Gaussian curvatures of the surface maximums ($\overline{\kappa}_c$) as the scale characterization parameter, the fine details (fluctuations with larger curvatures) are filtered out in turn along the decomposition process adaptively. The details of the SEMD algorithm were described in our previous work [57] and the corresponding program is available online [58]. Based on this decomposition, the influence of multiscale surface fluctuations on the dispersion force can be studied (Sec. III B).

For the traditional Euclidean descriptors, we draw on recent researches in the field of geotechnical engineering on the morphological characterization of soil particles

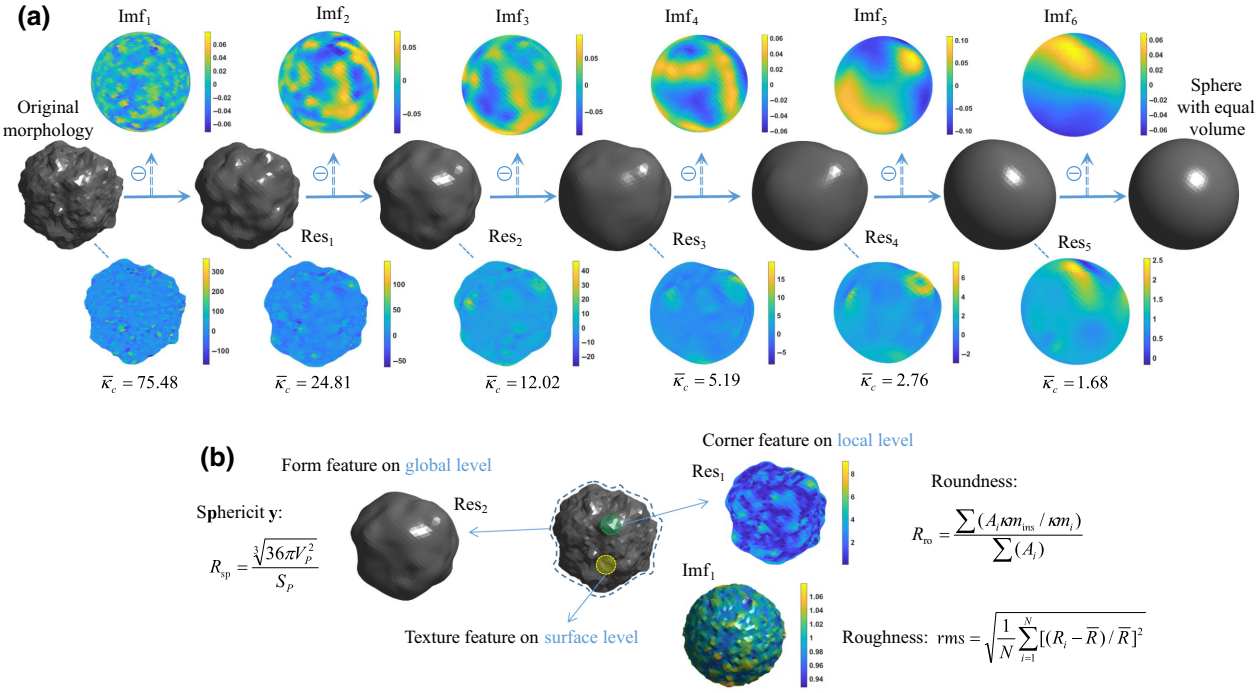

FIG. 1. Characterization of particle geometry. (a) Example of scale decomposition using SEMD. The top row shows the intrinsic mode function (Imf_i) corresponding to each order of decomposition, i.e., the part that is adaptively filtered out; the middle row shows the residual shape (Res_i) after filtering; and the last row shows the Gaussian curvature (see Ref. [61] for a detailed definition) distribution of the residual shape, with the average of the Gaussian curvatures of the surface maximums ($\bar{\kappa}_c$) taken as the scale characterization parameter. (b) Schematic of the three descriptors: sphericity for the global form feature, roundness for the local corner feature, and roughness for the surface texture feature. See Appendix A for detailed definitions of the descriptors.

[59,60]. As shown in Fig. 1(b), three descriptors at three observation levels are selected to comprehensively characterize the particle morphology, including sphericity for the global level, roundness for the local level, and roughness for the surface level. Here, to prevent interactions among the different observation levels, we first filtered the surface using the aforementioned SEMD before calculating the values of each descriptor (for details, see Ref. [57] and Appendix A). In Sec. III C, we establish relationships between the dispersion forces and these common descriptors by performing a large number of numerical calculations on particles with different morphologies.

B. Exact numerical model for the dispersion force beyond the additivity assumption

To study the influence of particle geometry on dispersion forces, we need to handle many particles with different complex morphologies, which requires a sufficiently flexible computational framework that can handle various morphologies. The FSC technique, a unified formalism capable of handling arbitrary materials in various geometries [62,63], is the best nonadditivity algorithm for investigating this problem.

The FSC algorithm is a well-established algorithm, and the critical elements of this technique are introduced below. As shown in Fig. 2, two neutral compact objects placed in a vacuum derive their dispersion force according to the surrounding fluctuating electromagnetic field. In the absence of any external force field, the average value of any single field component vanishes; however, the average values of the off-diagonal products of the field components are generally nonzero and may be related to a force density [the fluctuation-averaged Maxwell stress tensor (T_{ij})] that we can use to compute the dispersion forces.

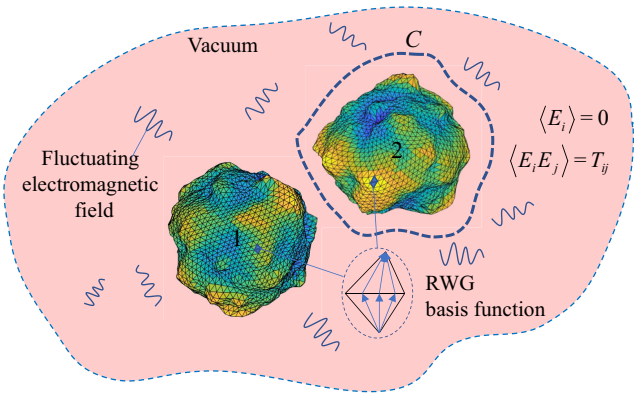

FIG. 2. Schematic depiction of the FSC algorithm.

As shown in Fig. 2, the i-directed dispersion force on compact object 2 can be determined by integrating the fluctuation-averaged stress tensor over any closed bounding surface C surrounding this body:

$$\mathcal{F}_i = \int_0^\infty \frac{d\xi}{\pi} F_i(\xi), \tag{1}$$

$$F_i(\xi) = \oint_C \langle T_{ij}(\mathbf{x},\xi)\rangle \hat{\mathbf{n}}_j(x) d\mathbf{x}. \tag{2}$$

Here, Eq. (1) indicates that the dispersion force can be obtained by integrating the contributions of all imaginary frequencies $\xi = i\omega$. In Eq. (2), $\hat{\mathbf{n}}_j(x)$ is the inward-directed unit normal to C at x, and the expectation value $\langle T_{ij}\rangle$ can be written in terms of the components of the electric and magnetic fields:

$$\begin{aligned} &T_{ij}(\mathbf{x},\xi) \\ &= \varepsilon(\mathbf{x},\xi)\left[\langle E_i(\mathbf{x})E_j(\mathbf{x})\rangle_\xi - \frac{\delta_{ij}}{2}\sum_k \langle E_k(\mathbf{x})E_k(\mathbf{x})\rangle_\xi\right] \\ &\quad + \mu(\mathbf{x},\xi)\left[\langle H_i(\mathbf{x})H_j(\mathbf{x})\rangle_\xi - \frac{\delta_{ij}}{2}\sum_k \langle H_k(\mathbf{x})H_k(\mathbf{x})\rangle_\xi\right]. \end{aligned} \tag{3}$$

Thus far, the calculation of the dispersion force has been reduced to calculating the fluctuation-averaged products of the field components at each imaginary frequency.

Crucial work by Lifshitz *et al.* in the 1950s [8,34] established the relationship between the fluctuation-averaged products of the field components and the scattering portions of the dyadic Green functions in classical electromagnetism based on the fluctuation-dissipation theorem:

$$\begin{aligned} \langle E_i(\mathbf{x})E_j(\mathbf{x})\rangle_\xi &= \hbar\xi \mathcal{G}_{ij}^{\mathrm{EE}}(\xi;\mathbf{x},\mathbf{x}'), \\ \langle H_i(\mathbf{x})H_j(\mathbf{x})\rangle_\xi &= \hbar\xi \mathcal{G}_{ij}^{\mathrm{MM}}(\xi;\mathbf{x},\mathbf{x}'). \end{aligned} \tag{4}$$

Here, $\mathcal{G}_{ij}^{\mathrm{EE}}(\xi;\mathbf{x},\mathbf{x}')$ and $\mathcal{G}_{ij}^{\mathrm{MM}}(\xi;\mathbf{x},\mathbf{x}')$ are the scattered portions of the electric and magnetic fields at x due to the current sources at x', respectively. According to Eq. (4), the calculation of the dispersion force can be completely reduced to solving the classical electromagnetic scattering problem. Therefore, various classical methods can be exploited to calculate the dispersion forces originating from quantum fluctuations, with a few important modifications. The key modification is the use of the so-called Wick rotation ($\xi = i\omega$) to stabilize the calculation, which ensures that all frequency-dependent quantities ($\varepsilon, \mu, \langle\,\rangle, \mathcal{G}$) in Eqs. (1)–(4) are considered in the imaginary frequency.

For scattering problems with homogeneous geometries embedded in homogeneous media, the boundary element method (BEM) can be applied to effectively use the known solutions of Maxwell's equations, thus greatly improving the computational efficiency. Therefore, the BEM rather than other computational electromagnetic methods (such as the finite difference or finite element methods) is used in the FSC algorithm. Taking perfectly electrically conducting bodies embedded in a vacuum as an example, the scattering part of the dyadic Green function $\mathcal{G}$ can be obtained with the BEM as

$$\begin{aligned} \mathcal{G}_{ij}^{\mathrm{EE}}(\xi;\mathbf{x},\mathbf{x}') &= -\sum_{\alpha\beta}\langle \Gamma_i^{\mathrm{EE}(\mathbf{x})}|f_\alpha\rangle [M^{-1}]_{\alpha\beta}\langle \Gamma_j^{\mathrm{EE}(\mathbf{x})}|f_\beta\rangle, \\ \mathcal{G}_{ij}^{\mathrm{MM}}(\xi;\mathbf{x},\mathbf{x}') &= -\sum_{\alpha\beta}\langle \Gamma_i^{\mathrm{ME}(\mathbf{x})}|f_\alpha\rangle [M^{-1}]_{\alpha\beta}\langle \Gamma_j^{\mathrm{EM}(\mathbf{x})}|f_\beta\rangle. \end{aligned} \tag{5}$$

Here, Γ denotes the vacuum dyadic Green functions and $\{f_\alpha\}$ refers to a set of localized tangential vector-valued basis functions depending on the surface discretization (i.e., the boundary elements); $\langle\Gamma|f_\alpha\rangle$ refers to the interactions between Γ and f_α, namely, $\int_{\mathrm{sup}\mathbf{f}_\alpha} \Gamma\cdot f_\alpha d\mathbf{x}$, and M is the BEM matrix, which describes the interactions among the basis functions in the exterior medium as $M_{\alpha\beta} = \int_{\mathrm{sup}\mathbf{f}_\alpha}\int_{\mathrm{sup}\mathbf{f}_\beta} f_\alpha(\mathbf{x})\cdot\Gamma^{\mathrm{EE}}\cdot f_\beta(\mathbf{x}')d\mathbf{x}d\mathbf{x}'$.

Equation (5) can be used to calculate $\mathcal{G}$ at each point on the closed bounding surface $\mathcal{C}$; thus, the dispersion force can be obtained via integration. However, Reid and Johnson [63] carried out a further analytical derivation based on Eq. (5), simplifying the calculation of the dispersion force as a compact matrix-trace formula.

Substituting Eq. (5) into Eq. (2), according to the symmetry of M, the dispersion force at a certain frequency can be written as

$$\begin{aligned} F_i(\xi) = \frac{\hbar}{2} Z_0 \kappa \sum_{\alpha\beta}[M^{-1}]_{\alpha\beta}\int_{\mathrm{sup}\mathbf{f}_\alpha} d\mathbf{r}\int_{\mathrm{sup}\mathbf{f}_\beta} d\mathbf{r}' f_{\alpha k}(\mathbf{r}) \\ \cdot\bar{\mathcal{L}}_{ikl}(\mathbf{r},\mathbf{r}')\cdot f_{\beta l}(\mathbf{r}'), \end{aligned} \tag{6}$$

where $\bar{\mathcal{L}}_{ikl}(\mathbf{r},\mathbf{r}')$ is a symmetrized version of the integral kernel along the closed bounding surface $\mathcal{C}$, which has the special property

$$\bar{\mathcal{L}}_{ikl}(\mathbf{r},\mathbf{r}') = \begin{cases} 0 & \text{if } \mathbf{r},\mathbf{r}' \text{ lie on the same side of } \mathcal{C}, \\ \dfrac{\partial}{\partial \mathbf{r}_i^I} G_{kl}(\mathbf{r}^I - \mathbf{r}^E) & \text{if } \mathbf{r},\mathbf{r}' \text{ lie on opposite side of } \mathcal{C}, \end{cases} \tag{7}$$

where G refers to the photon Green function and $\mathbf{r}^I$ ($\mathbf{r}^E$) indicates whether $\mathbf{r}$ and $\mathbf{r}'$ lie in the interior (exterior) of $\mathcal{C}$. According to Eq. (7), for the case shown in Fig. 2, the integral kernel $\bar{\mathcal{L}}$ is nonzero only when f_α and f_β are on the surfaces of particles 1 and 2, respectively. Based on this

special property, Eq. (6) can be reduced to the matrix-trace form

$$F_i(\xi) = -\frac{\hbar}{2}\mathrm{Tr}\left\{\mathbf{M}^{-1}\cdot\frac{\partial\mathbf{M}}{\partial\mathbf{r}_i}\right\}. \tag{8}$$

Then, the full dispersion force in Eq. (1) becomes

$$\mathcal{F}_i = -\frac{\hbar}{2}\int_0^\infty d\xi\,\mathrm{Tr}\left\{\mathbf{M}^{-1}\cdot\frac{\partial\mathbf{M}}{\partial\mathbf{r}_i}\right\}. \tag{9}$$

At this point, the calculation of the dispersion force is finally reduced to calculation of the BEM matrix M. For general materials, the derivation is similar, and the final formulae have the form shown in Eq. (9), except that M needs to be replaced by the Poggio-Miller-Chang-Harrington-Wu matrix.

The solution of the BEM matrix requires a reasonable surface discretization and the corresponding localized basis functions. As shown in Fig. 2, the surfaces of compact objects can be discretized by Delaunay triangulation, and the Rao-Wilton-Glisson basis functions [64] based on two adjacent triangular planes are applied in the FSC algorithm. For the present study, this choice has the additional benefit of sharing the same set of meshes with the aforementioned morphological analysis.

The above description allows the dispersion force to be computed at zero temperature $T = 0^+$. In the case of a nonzero temperature ($T > 0$), the description can be modified by converting the integral in Eq. (9) into a sum over a series of discrete imaginary frequencies:

$$\mathcal{F}_i = \frac{2\pi k_B T}{\hbar}\sum_{n=0}^{\infty}{}' F_i(\xi_n), \qquad \xi_n = n\frac{2\pi k_B T}{\hbar}. \tag{10}$$

Here k_B is Boltzmann's constant and $\sum'$ indicates a sum with weight $1/2$ for the $n = 0$ term. The frequencies $\xi_n = n2\pi k_B T/\hbar$ are known as Matsubara frequencies.

The accurate computation of the dispersion force using the FSC technique requires that accurate dielectric data of the materials are available. As shown in Eq. (10), theoretically, the contributions of different Matsubara frequencies to the full band must be calculated. For interbody distances at the micronanometer scale, frequencies in the ultraviolet (UV) region have a considerable impact on the dispersion force [30]. However, it is not possible to obtain tabulated dielectric data for all dispersive materials in the full band. Reviewing the available dielectric data, data in the infrared and visible regions are abundant, while data in the UV region are lacking. This data imbalance occurs because few techniques exist for measuring optical constants in the UV region [65]. Therefore, different ideal dielectric function models have been introduced to predict the frequency without measurement data, such as the Drude model, plasma model, Lorentz model, and Ninham-Parsegian model, which have been commonly used in recent studies. In addition to these models, an empirical modified harmonic oscillator model was recently introduced by Moazzami Gudarzi and Aboutalebi [65]. In this model, dielectric data of 55 common materials obtained from different sources were compiled and evaluated according to optical sum rules and Kramers-Kronig relations to ensure internal consistency. On the basis of these data and the optical band gap, density, and chemical composition of the materials, the model parameters can be accurately determined. The accuracy of this dielectric function model was validated by the experimentally measured dispersion force in a planar configuration. The general form of the model can be expressed as

$$\varepsilon(\xi_n) = 1 + \begin{cases} \displaystyle\sum_j \frac{C_j}{1+(\xi/\omega_j)^{\alpha_j}}, & j \le 3, \\ \displaystyle\frac{C_{\mathrm{UV}}}{1+(\xi/\omega_{\mathrm{UV}})^{\alpha_{\mathrm{UV}}}} + \frac{\omega_p^2}{\xi^2+\gamma\xi}, & \end{cases} \tag{11}$$

in which the first equation applies to semiconductors and insulators, while the second equation applies to metals. Here, we select four materials with different properties, namely, Au (metal), Si (semiconductor), SiO_2 (inorganic insulator), and $(C_2H_4)_n$ (organic insulator), and calculate the dispersion force under complex morphology. The specific details of the dielectric functions can be found in the original literature of Moazzami Gudarzi and Aboutalebi [65].

After addressing the nonadditivity and dielectric functions, the only remaining factor that may affect the accuracy is the discrete error in the numerical calculation. In Appendix B, we provide a detailed discretization study under different geometric configurations. Considering the efficiency, the number of surface triangles is set to 5000, and the accuracy can be guaranteed when the surface curvature $\overline{\kappa}_c < 100$.

C. Geometric configurations in the computational implementation

To study the influence of particle geometry on dispersion forces, data of real particles with varying morphologies are first needed. To generalize the calculations and obtain sufficient ranges for each characterization parameter, a numerical method proposed by Wei *et al.* [66] for randomly constructing real particles with different morphologies is employed.

Unlike spheres, arbitrary shapes are anisotropic, resulting in two problems: the definition of the distance between particles is uncertain, and the geometric configuration changes as the particles rotate. In practical applications, we are concerned with the mean and standard deviation of

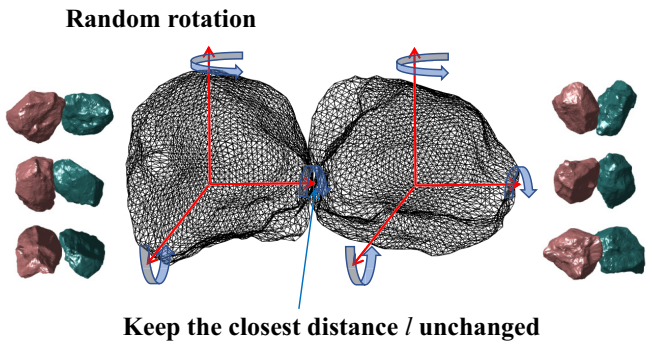

FIG. 3. Geometric configurations in the computational implementation for the arbitrary particles. The middle schematic shows the random rotation of two particles along three axes while keeping the closest distance l between the two particles constant. The left- and right-hand side schemata show examples after random rotation.

the dispersion forces. As shown in Fig. 3, we maintain the closest distance l between the particles, which we define as the distance between the particles, and calculate the mean and standard deviation of the dispersion force by randomly rotating the particles to produce different configurations. In addition, if not otherwise specified, two identical particles interacting with each other are employed throughout the calculations.

III. RESULTS AND DISCUSSION

A. Comparison between additivity and nonadditivity methods

For regular geometries, previous literature has extensively compared additivity and nonadditivity methods. Here, for particles with complex shapes, we present a quantitative comparison between additivity and nonadditivity methods. Schematic diagrams of two commonly used algorithms (PWS approximation and PFA) based on the additivity assumption are shown in Fig. 4(a). For the PWS technique, we use a modified version of the Hamaker summation approximation by considering Lifshitz theory and the Clausius-Mossotti relation [13]. In this algorithm, the potential energy originating from the dispersion force between particles A and B can be expressed as

$$G_{AB}(T)_{\mathrm{PWS}} = -\frac{\hbar}{\pi}\left(\frac{3}{4\pi}\right)^2 \int_{V_A} d^3_{r_A} \int_{V_B} d^3_{r_B} \sum_{n=0}^{\infty}{}' g(\xi_n), \tag{12}$$

$$g(\xi_n) = \left(\frac{\varepsilon(i\xi_n)-1}{\varepsilon(i\xi_n)+2}\right)^2 \left[\frac{3}{r^6} + \left(\frac{\xi_n}{c}\right)\frac{6}{r^5} + \left(\frac{\xi_n}{c}\right)^2 \frac{5}{r^4} + \left(\frac{\xi_n}{c}\right)^3 \frac{3}{r^3} + \left(\frac{\xi_n}{c}\right)^4 \frac{1}{r^2}\right] e^{-2\xi_n r/c}. \tag{13}$$

The $\{\xi_n\}$ are the Matsubara frequencies at temperature T, as shown in Eq. (10), and r refers to the distance between the two cubes $d^3_{r_A}$ and $d^3_{r_B}$. The dispersion force is obtained by taking the spatial derivative of $G_{AB}(T)_{\mathrm{PWS}}$. This calculation takes into account the dispersion property, retard effect, and temperature correction. For the PFA algorithm, the potential energy per unit area in the plane-plane configuration must be determined first, the exact solution of which was derived by Lifshitz *et al.* [67]:

$$G_{\mathrm{pp}}(T,l) = \frac{k_B T}{2\pi} \sum_{n=0}^{\infty}{}' \int_0^{\infty} k_\perp dk_\perp \times \sum_{\alpha=\mathrm{TE,TM}} \ln[1 - r^2_\alpha(i\xi_n, k_\perp) e^{-2lq_n}]. \tag{14}$$

Here $k_\perp$ denotes the magnitude of the projection of the wave vector onto the plane of the plates, $r_\alpha(i\xi_n, k_\perp)$ denotes the Fresnel reflection coefficient for the two independent polarizations $\alpha = \mathrm{TE, TM}$ of the electromagnetic field, l refers to the distance between the two planes, and $q_n = \sqrt{\xi_n^2/c^2 + k_\perp^2}$. The dispersion property, retard effect, and temperature correction are also considered in this analytical solution. Then, the total potential energy between the curved surfaces is obtained by summing the potential energy of each plane-plane configuration:

$$G_{AB}(T)_{\mathrm{PFA}} = \sum G_{\mathrm{pp}}(T, l_i)\Delta S_i \tag{15}$$

with l_i and ΔS_i denoting the distance between and the surface area of each plane-plane configuration of the curved surfaces, respectively, as shown in Fig. 4(a). Finally, the dispersion force is obtained by taking the spatial derivative of $G_{AB}(T)_{\mathrm{PFA}}$.

In this comparative study, the optimal versions of both additivity algorithms are used, taking into account corrections for factors other than geometry. Moreover, the computational complexity of the PWS algorithm is $O(L^6)$ (L refers to the linear resolution of the volume integral). However, for particles with complex shapes, the computational complexity becomes unacceptable if the resolution is large enough to capture boundary variations. Thus, we propose a multidomain partitioning approach, as shown in Fig. 4(a). With this approach, the computational complexity is significantly reduced to an acceptable level. The optimized programs for the two additivity algorithms are available online [68].

A specific configuration with a specific complex-shaped particle (the three geometric descriptors are $R_{\mathrm{sp}} = 0.9393$, $R_{\mathrm{ro}} = 0.5104$, $\mathrm{rms} = 0.0218$) is used to perform comparison study. The radius R of the sphere with the same volume as the particle is taken to characterize the particle size, which is set here as $R = 1$ μm. The rotation

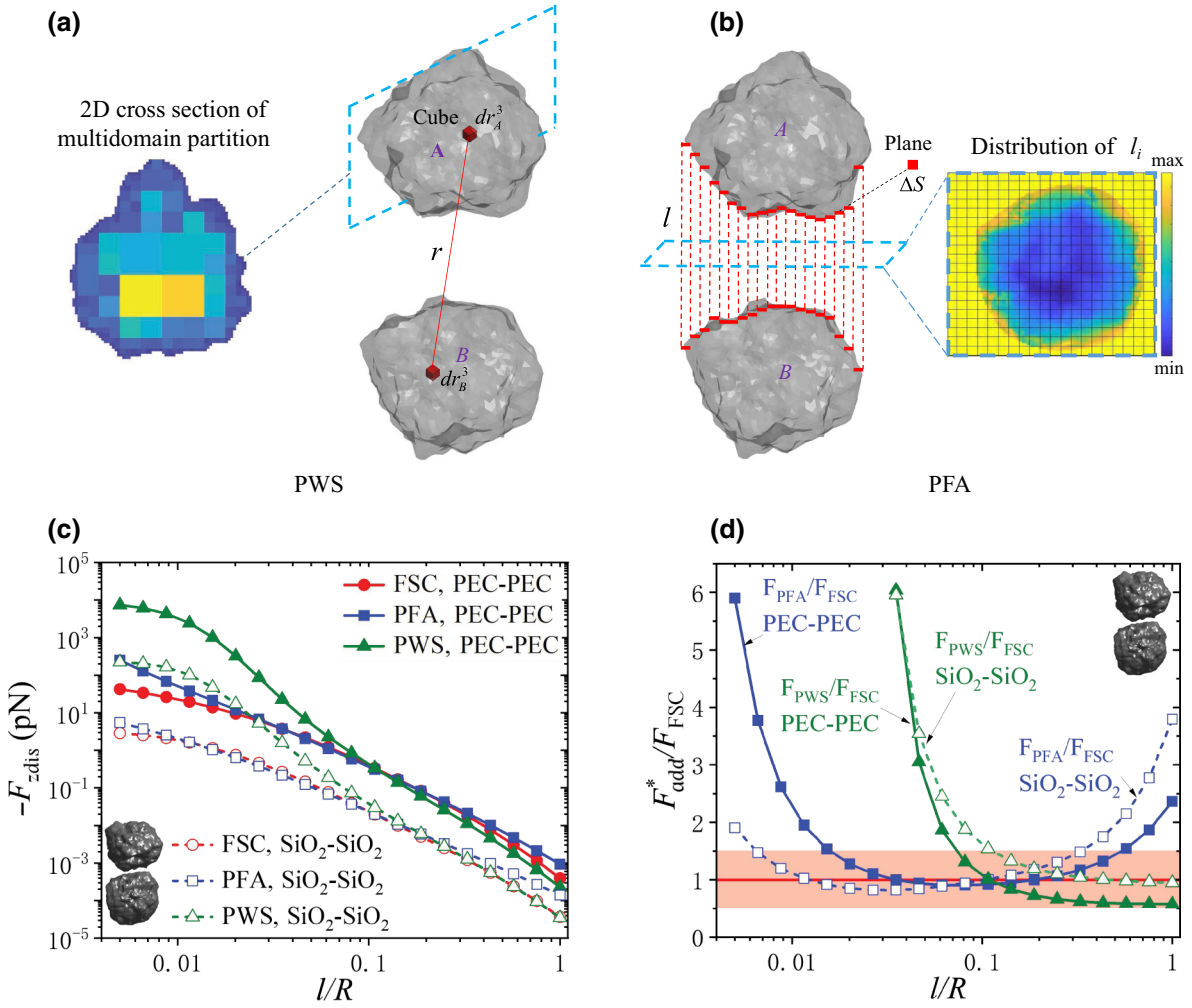

FIG. 4. Comparison between additivity and nonadditivity methods. (a) Schematic of the PWS algorithm, with the left 2D cross section showing the proposed multidomain partition approach. (b) Schematic of the PFA algorithm, with the right contour showing the distribution of the distance between each plane-plane configuration of the two curved surfaces. Panels (c) and (d) show comparisons between the computed results of the three algorithms, where (c) shows the calculated dispersion forces and (d) shows the results of normalizing the two additive algorithms using FSC.

angle of two interacting particles is set randomly and kept constant, and the closest distance l between the particles is changed in the calculation. The materials are set to a perfectly electrically conducting (PEC) metal and a dispersive medium SiO_2, and the temperature is set to room temperature (298.15 K). A comparison of the three algorithms as the distance changes is shown in Figs. 4(c) and 4(d). Overall, compared to the exact nonadditivity algorithm, the additivity algorithms overestimate the dispersion force. For complex-shaped particles, the PFA technique performs better than the PWS approach. The relative errors in the PFA and PWS methods can reach up to about 10 times and about 1000 times, respectively. For each additivity algorithm, the error trends of the PEC and dispersive medium are consistent. For the PFA technique, the error at intermediate distances is relatively small, while for the PWS method, the error is smaller at longer distances. If 50% is taken as the acceptable error threshold, the relative distance (l/R) ranges for the PFA and PWS techniques to satisfy this threshold are approximately $[0.02, 0.2]$ and $[0.2, 1]$.

B. Influence of multiscale surface fluctuations on the disperse force

As described in Sec. II A, the complex morphology of a real particle can be regarded as a superposition of surface fluctuations at different scales. The SEMD algorithm, which is an adaptive spatial filter, can be applied to sequentially filter surface fluctuations at different scales from fine to coarse. With the average of the Gaussian curvatures of the surface maximums ($\overline{\kappa}_c$) taken as the scale characterization parameter, the influence of multiscale surface fluctuations on the disperse force can be quantitatively

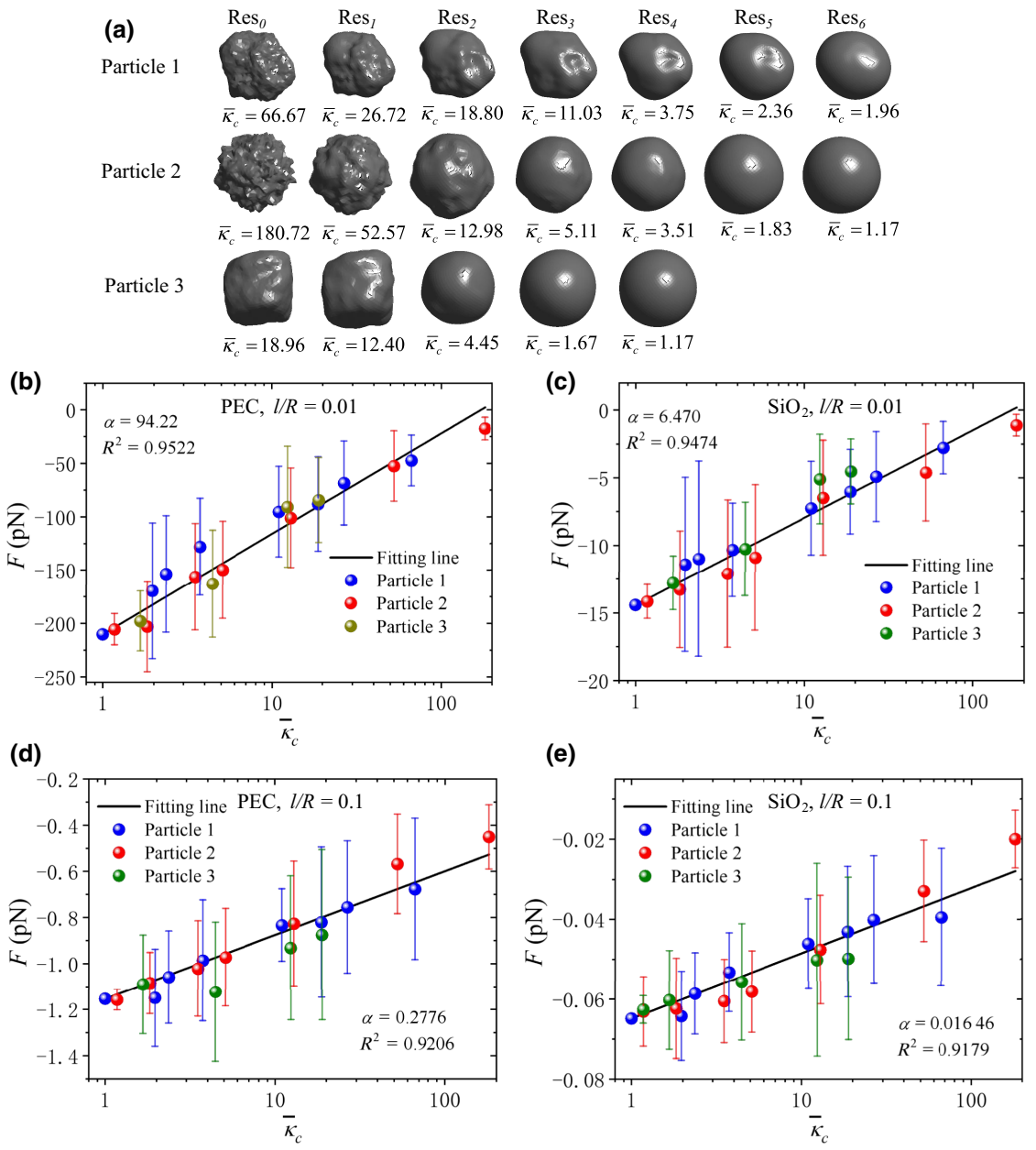

FIG. 5. Influence of multiscale surface fluctuations on the disperse force. Panel (a) shows the residual shapes at each order of the decomposition of three selected particles. Panels (b)–(e) show the variations of the dispersion force with the mean Gaussian curvature ($\bar{\kappa}_c$) for particles with surface fluctuations of different scales at different distances and materials. The colored dots represent the average of the cases generated by random rotation as shown in Fig. 3, and the error bars refer to their standard deviations. Two identical particle interactions are used for all cases.

studied by calculating the force of each residual shape obtained by the SEMD algorithm.

As shown in Fig. 5(a), three particles with large morphological differences are randomly selected, and their residual shapes at each order are obtained with the SEMD algorithm. The materials are set to PEC and SiO_2, and the temperature is set to room temperature (298.15 K). The distances between the particles are set to $l/R = 0.01, 0.1,$ and 1. As described in Sec. II C, for cases with different distances, shapes, and materials, a sufficient number of configurations must be obtained through random rotations. By testing different cases, we find that the mean and standard deviation of the dispersion force stabilize when the particles are randomly rotated more than 10 times; thus, we choose to randomly rotate the particles 20 times for each case.

Figures 5(b)–5(e) show the results for $l/R = 0.01$ and 0.1. When $l/R = 1$, there is little difference in the dispersion forces of the different shapes, and these results are provided in Appendix C. The dispersion force decreases with increasing mean Gaussian curvature ($\overline{\kappa}_c$), and the mean value of the dispersion force and the logarithm of $\overline{\kappa}_c$ show a good linear correlation. Taking the dispersion force between spheres (F_{ss}) with equal volumes (i.e., the case of $\overline{\kappa}_c = 1$) as the intercept, the linear fitting results in Figs. 5(b)–5(e) all have R^2 values greater than 0.9. Therefore, the following relationship between the mean of the dispersion force and $\overline{\kappa}_c$ can be established:

$$F(T, l/R) = \alpha \lg(\overline{\kappa}_c) + F_{ss}(T, l/R) \tag{16}$$

with α an empirical parameter that is determined by the distance and material. The dispersion force gradually becomes insensitive to the morphology as the distance increases. When $l/R = 0.01$, the variation range ($|F_{max}|/|F_{min}|$) is approximately 15 times; when $l/R = 0.1$, $|F_{max}|/|F_{min}| \sim 3$; and when $l/R = 1$, the variation range remains essentially constant.

Although the material significantly affects the magnitude of the dispersion force, it has little effect on the variation trend. Normalizing Eq. (16) by $F_{ss}(T, l/R)$ gives

$$F_r = 1 + \beta \lg(\overline{\kappa}_c), \tag{17}$$

where $F_r = F/F_{ss}$ and $\beta = \alpha/F_{ss}$. When $l/R = 0.01$, $\beta = -0.4496$ for the PEC and -0.4489 for SiO_2. When $l/R = 0.1$, $\beta = -0.2406$ for the PEC and -0.2537 for SiO_2. When $l/R = 1$, $\beta \to 0$ for both materials. Thus, different materials have little effect on the value of β.

The error bars in Fig. 5 represent the standard deviations for each random rotation case. The ratio of the standard deviation to the mean value is taken as the relative error δ_r, without distinguishing the material, and its variation with the morphology is shown in Fig. 6. As the curvature increases, the relative error increases. Moreover, as the distance decreases, the relative error increases. Using $[\lg(1 + \lg \overline{\kappa}_c)]/a$ as the fitting function, the R^2 values exceed 0.65. The mean $\overline{\delta}_r$ and standard deviation $\sigma_{\delta r}$ are used to quantify the statistical characteristics of the relative error at different distances. When $l/R = 0.01$, $\overline{\delta}_r \pm \sigma_{\delta r} = 0.4296 \pm 0.2055$. When $l/R = 0.1$, $\overline{\delta}_r \pm \sigma_{\delta r} = 0.2614 \pm 0.1244$. With these values, we can determine to what extent the geometric anisotropy affects the discreteness of the dispersion force. In addition, the mean of the relative error $\overline{\delta}_r$ is positively correlated with the aforementioned $|\beta|$ defined in Eq. (17).

By performing an exact numerical study, the influence law of multiscale surface fluctuations on the dispersion force is obtained quantitatively. In summary, the dispersion force decreases as the curvature increases, the shape sensitivity of the force decreases as the distance increases, and the material has little effect on the change trend. Taking the dispersion force between spheres with the same volume and material as a reference, the effect of the morphology and distance can be expressed as a simple empirical equation, as shown in Eq. (17). As the irregularity in the shape increases and the distance decreases, the discreteness of the force increases due to geometric anisotropy, and the range of the variation of the relative error is shown in Fig. 6.

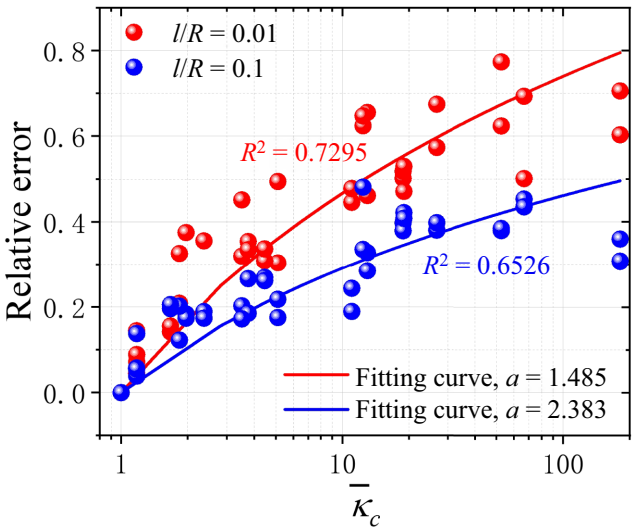

FIG. 6. Variation of the relative error with mean Gaussian curvature at different distances.

C. Multistage approximation of the dispersion force of real particles

The nonadditivity algorithm is accurate but has a considerable computational cost. When the distance is small, UV frequencies have substantial contributions; thus, many Matsubara frequencies need to be calculated for the force calculation to converge (e.g., when $R = 1$ μm, $l/R = 0.01$, 500 orders are needed). In practice, it is difficult to perform accurate calculations for different particles with various morphologies. Therefore, establishing a law and providing a prediction formula for the dispersion force based on the exact numerical study are both valuable.

Until now, an exact analytical solution of this force has been limited to the Lifshitz solution in the plane-plane configuration [as shown in Eq. (14)]. According to the PFA method, the dispersion force in the sphere-sphere configuration can be expressed as a function of the radius and the energy in the plane-plane configuration:

$$F_{ss}^{PFA}(T, l/R) = \pi R G_{pp}(T, l). \tag{18}$$

Here, we consider two spheres with the same radius R. Unfortunately, the PFA approach is effective only for limited distances and curvatures. As a result, the "beyond PFA correction" was proposed and discussed in

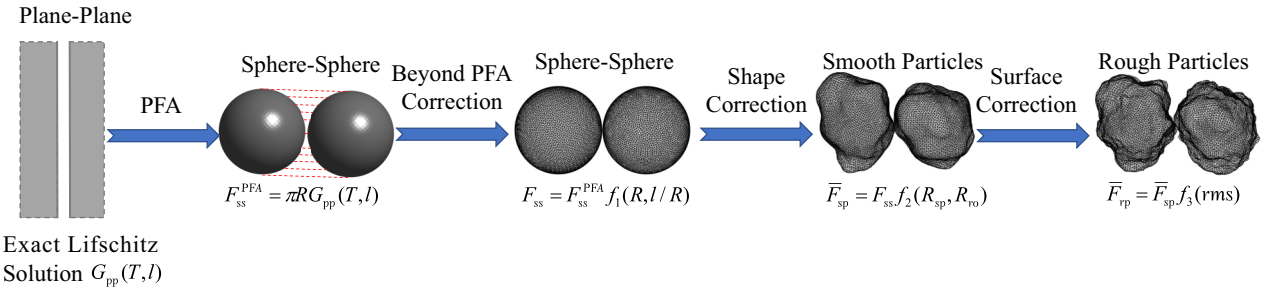

FIG. 7. Schematic diagram of the multistage correction of the real particle dispersion force, where $f_i(\cdot)$ refers to the correction function of each stage to be determined.

Refs. [69–71]. The basic idea of the beyond PFA correction is to multiply the PFA solutions by a correction factor according to the geometric descriptors. Based on this idea, we propose a multistage correction method for predicting the dispersion forces of real particles, as illustrated in Fig. 7. Equation (18) gives the first PFA correction to the Lifshitz solution (G_{pp}) in the sphere-sphere configuration (F_{ss}^{PFA}), and the remaining correction stages are discussed below.

From F_{ss}^{PFA} to F_{ss}. Previous studies [71,72] have focused on this stage. According to the derivative expansion approach, the leading correction has the form

$$\frac{F_{ss}}{F_{ss}^{PFA}} = 1 + \alpha_{ss}\frac{l}{R} + \cdots, \tag{19}$$

where the coefficient α_{ss} is independent of R. Previous studies have indicated that the distance is mainly restricted to the range of $l/R \sim [0.1, 1]$ and that the dielectric function is restricted to the Drude and plasma models. As a result, the range of α_{ss} and the form of subleading corrections remain controversial.

Here, we consider a wider range of distances ($[0.005, 2]$) with the FSC algorithm and more materials [PEC, Au, SiO_2, Si, $(C_2H_4)_n$] using the modified empirical harmonic oscillator model proposed by Moazzami Gudarzi and Aboutalebi [65]. The calculation results are given in Fig. 8. Taking the distances (l/R) on logarithmic coordinates, we find that the curves of F_{ss}/F_{ss}^{PFA} show bell-shaped characteristics. Fitting with the Gaussian function, the R^2 can all reach above 0.97. Therefore, from F_{ss}^{PFA} to F_{ss}, we use the Gaussian function in logarithmic coordinates as the new correction function, i.e.,

$$\frac{F_{ss}}{F_{ss}^{PFA}} = \alpha_{ss1}\exp\left[-\frac{(lx-\alpha_{ss2})^2}{2\alpha_{ss3}^2}\right], \qquad lx = \lg(l/R), \tag{20}$$

where α_{ss1}, α_{ss2}, and α_{ss3} are parameters to be determined. It can be seen that these parameters depend mainly on the type of material, and they are also related to R, but have little influence. Therefore, the effect of R is ignored in this study, and the values of these parameter for the five materials are provided in Table I by fitting all radii together.

From F_{ss} to F_{sp}. This correction is the main work of this study. Equation (17) obtained in the Sec. III B is an acceptable correction. However, in practice, three-level descriptors are more commonly used to characterize the morphology, where sphericity and roundness represent the global form and local corner features, respectively. As mentioned before, the curvature that can be accurately calculated at finite resolution is limited considering the

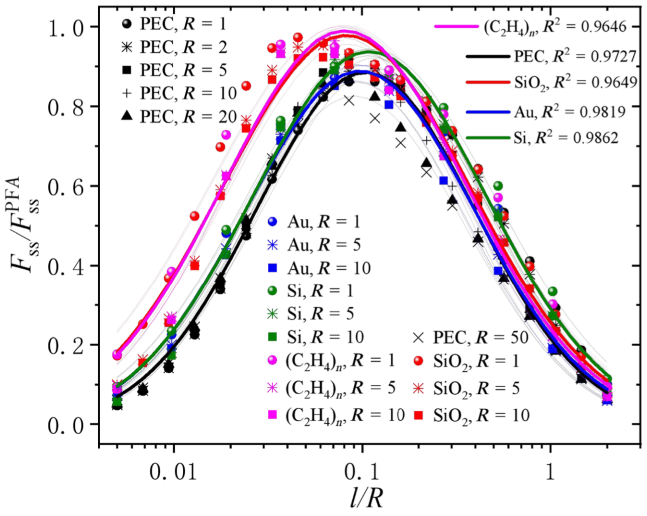

FIG. 8. Variation of the ratio of F_{ss} (obtained by FSC) and F_{ss}^{PFA} (obtained by PFA) with distance between two spheres with equal radius, and their corresponding curve fittings. The same material is used for the two interacting spheres.

TABLE I. Fitting parameters for different materials.

	Material				
	PEC	SiO_2	Au	Si	$(C_2H_4)_n$
α_{ss1}	0.8851	0.9782	0.8885	0.9374	0.9895
α_{ss2}	−0.9826	−1.0844	−1.0106	−0.9607	−1.0920
α_{ss3}	00.8623	0.9359	0.8615	0.8865	0.9171

computational load. The SEMD-based three-level classification can filter out the influence of surface fluctuation to obtain "smooth particles" with the same sphericity and roundness as the original morphology, and their curvature is in the range that can be accurately calculated. By calculating a large number of "smooth particles" with different sphericity and roundness, the shape correction from F_{ss} to F_{sp} can be obtained.

Here, 13 particles with widely different morphology are chosen [as shown in Fig. 9(a)], and the temperature is set to room temperature (298.15 K). The same as the previous section, 20 random rotations are performed for each case. Taking the materials as PEC and SiO_2, the results when $l/R = 0.01$ are shown in Fig. 9(b). It can be seen that the relationship

$$\frac{F_{sp}}{F_{ss}} = 1 + \alpha_{sp}\left(\frac{R_{sp} + R_{ro}}{2} - 1\right) \tag{21}$$

holds, where α_{sp} is the only coefficient to be determined. The coefficient is not sensitive to the materials and depends mainly on the distance. By considering different distances between the smooth particles of the PEC material, the relationship between the coefficient α_{sp} and the relative distance is obtained, as shown in Fig. 9(c). As the distance increases, α_{sp} decays exponentially, i.e., the effect of shape on the force decays exponentially. When $l/R > 1$, it can be assumed that the shape has no effect on the force, and F_{ss} can be used instead of $\overline{F}_{sp}$.

From F_{sp} to F_{rp}. The correction at this stage is consistent with the roughness correction in previous studies [10,73,74]. The difference is that the influence of the surface fluctuations with smaller curvatures have been taken into account in the previous stages of this study, so that the correction at this stage can be controlled at the level of "perturbation." It should be noted here that the descriptor of surface texture depends on the resolution of the morphological data. The SEMD in this study decomposes the cross-linkage between surface and shape features of the particles, i.e., the resolution of the morphological data does not affect the shape descriptors, but does affect the surface descriptor. As discussed before, the resolution calculated

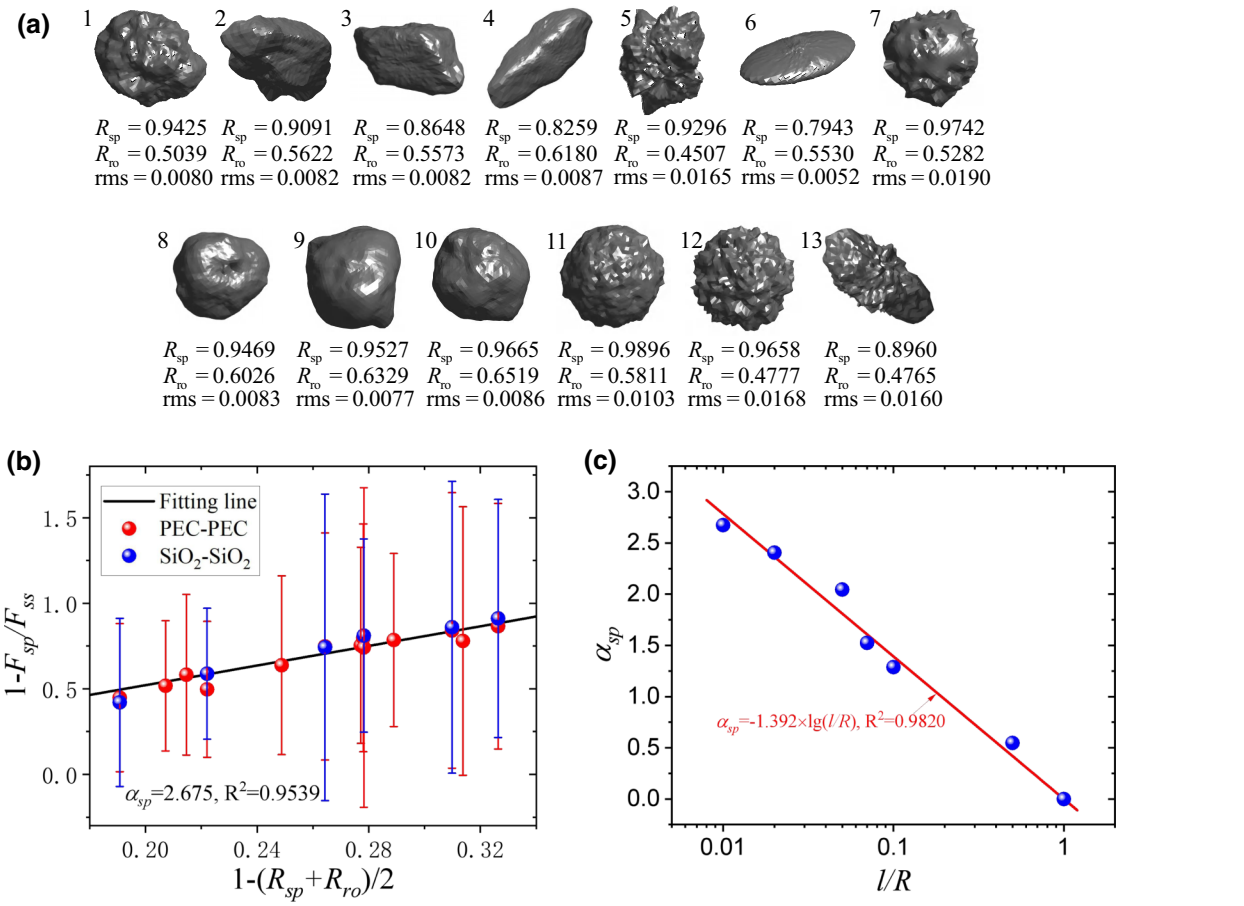

FIG. 9. Shape correction of dispersion force between arbitrarily shaped particles. Panel (a) shows the widely different morphologies of the selected particles. Panel (b) shows the excellent linearity between $1 - F_{sp}/F_{ss}$ and $1 - (R_{sp} + R_{ro})/2$, and the error bar refers to the relative error (standard deviation or mean) generated by the random rotation. Panel (c) shows the relationship between parameter α_{sp} and relative distance l/R. Two identical particle interactions are used for all cases.

in this study is limited to 5000 surface triangular cells ($\overline{\kappa}_c < 200$), and the roughness obtained by SEMD filtering is mainly concentrated between 0.007 and 0.009. Taking the average for all the cases, we get $\langle |F_{\rm rp} - F_{\rm sp}| / |F_{\rm rp}| \rangle = 0.9794$, which means that the error caused by surface texture is within 2.1%. Considering the limited range of roughness variation and the small error, the classical roughness perturbation correction formula [75] is directly adopted here, which can be expressed as

$$\frac{F_{\rm rp}}{F_{\rm sp}} = 1 + \alpha_{\rm rp} {\rm rms}^2, \tag{22}$$

where $\alpha_{\rm rp}$ is the only coefficient to be determined, which satisfies $\alpha_{\rm rp} \propto (l/R)^{-2}$.

In summary, the dispersion force between complex shaped particles can be predicted from the exact Lifshitz solution by the multistage corrections. By combining Eqs. (18), (20), (21), and (22), the final form of the prediction formula can be expressed as

$$F_{\rm rp} = \pi R G_{\rm pp}(T, l)\alpha_{\rm ss1} \exp\left[- \frac{(\lg(l/R) - \alpha_{\rm ss2})^2}{2\alpha_{\rm ss3}^2} \right] \times \left[1 + \alpha_{\rm sp}\left(\frac{R_{\rm sp} + R_{\rm ro}}{2} - 1 \right) \right](1 + \alpha_{\rm rp} {\rm rms}^2), \tag{23}$$

where the blue part refers to the exact Lifshitz solution, the red part refers to the PFA correction, the olive part refers to the beyond PFA correction of the sphere-sphere configuration, the magenta part refers to the shape correction, and the cyan part refers to the surface correction.

Factors influencing the dispersion force include geometry, material, and temperature. In the prediction formula (23), the influence of geometry is taken into account in the multistage corrections, while the influence of material and temperature are reflected in the exact Lifshitz solution. In fact, the three factors should be coupled, i.e., temperature and material affect the accuracy of the geometrical correction. To investigate the degree of influence of temperature and material, the dispersion force under different temperatures and materials for specific geometrical configurations is calculated.

Here, we choose two different configurations obtained by rotating the same particles ($R = 1$ μm) at the same relative distance ($l/R = 0.1$). Five representative materials are chosen, namely, PEC, SiO_2 , Au, Si, and $(C_2H_4)_n$ with temperatures varying from 0+ to their respective melting points [PEC, 2000 K; SiO_2, 1996.15 K; Au, 1337.15 K; Si, 1683.15 K; $(C_2H_4)_n$, 400 K]. According to Eq. (23), the ratio of the sphere-sphere PFA to the calculated FSC value can be taken to represent the geometrical correction, and the results are shown in Fig. 10. As can be seen from the figure, the magnitude of the change (standard deviation or mean) in the geometric correction factor caused by

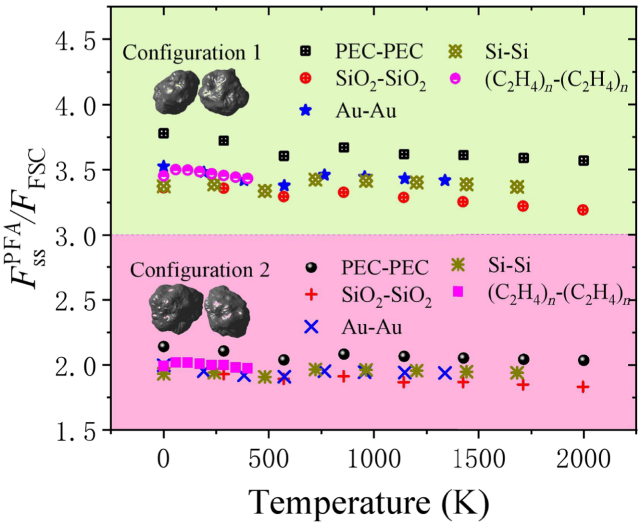

FIG. 10. Influence of the temperature and material on the accuracy of the geometrical correction.

material and temperature variations is 3.72% and 3.48% for the two geometric configurations, respectively. Compared with the several-fold changes caused by geometric changes, the changes caused by the coupling effect of material and temperature can be regarded as small fluctuations and can be neglected. This shows that the accuracy of Eq. (23) is acceptable when the effects of the three factors are considered in a decoupled manner, while ensuring enough efficiency.

To further verify the validity of Eq. (23), more examples of different materials with different morphologies at different temperatures are added, and the calculated values by FSC and predicted values by Eq. (23) of all cases are shown in Table II for comparison. It can be seen that the prediction error of the mean dispersion force is basically within 15% for the particles with complex morphology. Compared with the sphere-sphere PFA ($\pi R G_{\rm pp}$) commonly used in engineering, the error is reduced significantly, but the computational complexity is not increased. This indicates that Eq. (23) is a reasonable prediction. One can conveniently predict the mean dispersion force with the knowledge of materials, temperature, and geometry descriptors, and the corresponding program can be found online [68].

Considering the computational load, the resolution of the calculations in this study is limited, so the above conclusions are guaranteed to be valid for a certain curvature range. However, due to the introduction of the SEMD method, we decouple and interconnect the shape and the surface. That is, up to the stage of shape correction, our conclusions are universal, regardless of the resolution of the real morphological data. Meantime, the last remaining surface correction is guaranteed at the perturbation level. Therefore, for cases where the resolution exceeds

TABLE II. Comparison between the prediction by Eq. (23) and calculation by FSC. Considering the small impact, the roughness is uniformly taken as 0. The temperatures are chosen randomly between [0, 300] K, the radii are chosen randomly between [1, 10] μm, and the relative distances are chosen randomly between [0.01, 0.5]. The particle morphology corresponding to each ID are provided in Appendix D.

ID	Material	Temp. (K)	Radius (μm)	Distance (l/R)	Sphericity	Roundness	πRG_{pp} (pN)	Prediction (pN)	FSC (pN)	Error relative
1	PEC	170.7	1.191	0.0110	0.9199	0.5149	-701.5	-40.19	-35.18	0.1424
2	SiO_2	217.2	3.031	0.0944	0.9153	0.4807	-0.0112	-6.19×10^{-3}	-6.16×10^{-3}	0.0056
3	Au	83.84	3.159	0.0162	0.8976	0.5116	-12.87	-1.336	-1.227	0.0894
4	Si	209.7	5.317	0.1313	0.9241	0.5987	-6.49×10^{-3}	-4.27×10^{-3}	-4.87×10^{-3}	0.1250
5	$(C_2H_4)_n$	51.16	9.673	0.0987	0.9119	0.6299	-7.69×10^{-4}	-5.12×10^{-4}	-5.74×10^{-4}	0.1092
6	PEC	84.25	9.735	0.2078	0.8854	0.5861	-1.50×10^{-3}	-8.82×10^{-4}	-1.05×10^{-3}	0.1609
7	SiO_2	131.1	9.086	0.0741	0.7944	0.5952	-3.16×10^{-3}	-1.60×10^{-3}	-1.82×10^{-3}	0.1188
8	Au	109.0	4.639	0.0240	0.8076	0.7063	-2.538	-0.6207	-0.5373	0.1550
9	Si	158.3	7.997	0.1054	0.9243	0.5281	-2.589	-0.2364	-0.2445	0.0331
10	$(C_2H_4)_n$	8.192	2.101	0.0371	0.8937	0.5403	-0.2872	-0.1084	-0.1004	0.0797

the computational limits of this paper, the results of this study can be used for shape correction, and the existing perturbation approximation theory can be used for the last roughness correction.

IV. CONCLUSION

Geometric analyses and accurate calculations of the dispersion forces for particles with various complex shapes are provided, and the conclusions about the significance and reach of this work can be summarized as follows.

1. By comparing our approach with the optimal versions of the additivity algorithms, we find that the PFA and PWS approaches tend to overestimate the dispersion force for particles with complex shapes. With an error threshold of 50%, the relative distance (l/R) range for the PFA and PWS methods to satisfy this threshold are approximately [0.02, 0.2] and [0.2, 1].
2. We perform an exact numerical study for shapes with different curvatures obtained by an adaptive spatial filter, revealing that the average value of the dispersion force and the logarithm of the curvature show an excellent linear correlation.
3. Based on the results of large-scale nonadditivity calculations and multistage corrections, a convenient formula for predicting the dispersion force between complex-shaped particles from the exact Lifshitz solution is established.

Our work extends the study of the dispersion forces between micro- and nanoparticles with complex morphologies considering nonadditivity, improves the understanding of cohesion, and lays the foundation for a more reasonable contact model between irregular particles.

ACKNOWLEDGMENTS

This study is funded by the National Natural Science Funding of China (Grants No. 52104141, No. 12172230, No. U2013603, and No. 51827901), the Department of Science and Technology of Guangdong Province (Grant No. 2019ZT08G315), and the Guangdong Basic and Applied Basic Research Foundation (Grant No. 2023A1515012654).

The authors declare that there are no conflicts of interest regarding the publication of this article.

APPENDIX A: SEMD-BASED THREE-LEVEL DECOMPOSITION AND THE THREE CORRESPONDING DESCRIPTORS

In Ref. [57], we provide the general algorithm of SEMD. Based on the decomposed result of SEMD, the intrinsic mode functions (Imfs) can be artificially reclassified into

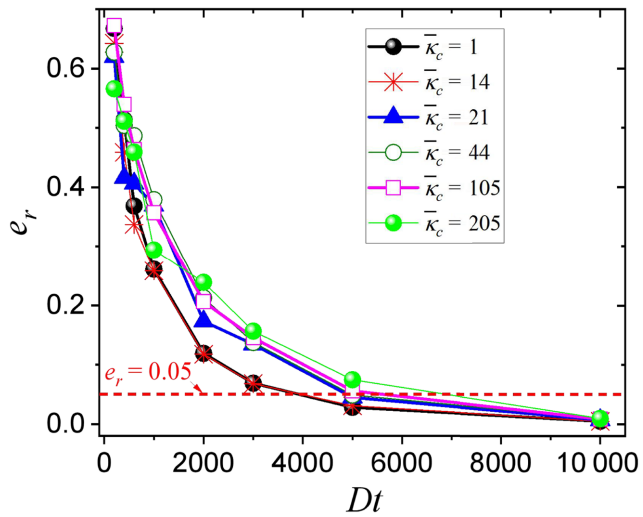

FIG. 11. Variation of the relative error with resolution.

TABLE III. Dispersion force between particles of different curvatures for PEC. "Curvature" refers to the average of the Gaussian curvatures of the surface maximums ($\overline{\kappa}_c$), and "SD" refers to the standard deviation.

	Curvature							
	66.67	18.80	3.75	1.97	1.00	180.73	12.98	3.51
Mean	-4.05×10^{-4}	-4.13×10^{-4}	-4.16×10^{-4}	-4.1×10^{-4}	-4.06×10^{-4}	-3.99×10^{-4}	-3.93×10^{-4}	-3.96×10^{-4}
SD	7.88×10^{-5}	7.41×10^{-5}	6.62×10^{-5}	5.69×10^{-5}	0	5.37×10^{-5}	4.03×10^{-5}	4.66×10^{-5}

a three-level decomposition by introducing differentiation criteria. The criteria can be flexibly selected according to the specific problem at hand [57].

Here, the specific averages of the Gaussian curvatures of the surface maximums ($\overline{\kappa}_c$) are taken as the criteria. The value of $\overline{\kappa}_c$ depends on the distance between extremas and the amplitude of this "waveform" and can therefore be regarded as a good scale-characterization parameter. Considering the specificity of the dispersion force, the three-level decomposition needs to satisfy the following two conditions.

(a) The effect of surface texture on the dispersion force needs to be "perturbation," and to meet this, the rms of the surface level needs to be less than 0.01.

(b) The object of the global level should be filtered out of all details, but keep the general shape unchanged.

Under the premise of satisfying the above two conditions, after many attempts, we finally found that using $\overline{\kappa}_c = 100$ and $\overline{\kappa}_c = 10$ as the surface-local level and local-global level differentiation criteria, respectively, would give reasonable decomposition results.

Based on the objects obtained by the three-level decomposition, the three-level descriptors can be calculated. For the global level, the classical sphericity defined by Wadell [51] is used, which is

$$R_{\mathrm{sp}} = \frac{\sqrt[3]{36\pi V_P^2}}{S_P}, \tag{A1}$$

where V_P and S_P are the volume and surface area of the particle, respectively. For the local level, the commonly used roundness is defined by Wadell [51]. Here, we use its modified version [53], which is

$$R_{\mathrm{ro}} = \frac{\sum(A_i \kappa m_{\mathrm{ins}}/\kappa m_i)}{\sum A_i}, \tag{A2}$$

where A_i is the area of the any triangular surface, that is, a part of the particle corners; κm_{ins} and κm_i are the mean curvatures of the maximum inscribed sphere and corner surface. For the surface level, the classical rms roughness is used here, which is defined as

$$\mathrm{rms} = \sqrt{\frac{1}{N}\sum_{i-1}^{N}[(R_i - \overline{R})/\overline{R}]^2}, \tag{A3}$$

where R_i refers to the radius of the surface-level object corresponding to each Fibonacci grid point (see Ref. [57] for the definition) on the sphere. All the basic parameters such as volume, area, curvature, etc. involved in the above equations can be obtained using the triangular-based algorithm [53,61], and the corresponding programs can be found online [58].

APPENDIX B: DISCRETIZATION STUDY

The discretization study is applied to particles of different curvatures. Residual shapes of different SEMD order for the same particle are chosen. The distance is set to $l/R = 0.1$, the material is set to PEC, the temperature is set to room temperature (298.15 K), and the calculation results for different grid resolutions Dt are shown in Fig. 2. The relative error e_r in the figure using

$$e_r = \frac{|F_{Dt} - F_\infty|}{|F_\infty|}, \tag{B1}$$

where F_{Dt} refers to the force calculated when the resolution is taken as Dt, and Dt here refers to the number of surface triangular elements. Here F_∞ refers to the exact value of the force when the resolution approaches infinity, which can obtained by the Richardson extrapolation

$$F_\infty = \frac{(Dt_2/Dt_1)^2 F_{Dt_2} - F_{Dt_1}}{(Dt_2/Dt_1)^2 - 1}, \tag{B2}$$

TABLE IV. Dispersion force between particles of different curvatures for SiO_2.

	Curvature							
	66.67	26.73	2.37	1.97	1.00	180.73	52.57	5.11
Mean	-3.95×10^{-5}	-4.01×10^{-5}	-4.27×10^{-5}	-4.35×10^{-5}	-4.16×10^{-5}	-3.79×10^{-5}	-3.98×10^{-5}	-4.17×10^{-5}
SD	7.18×10^{-6}	7.39×10^{-6}	3.94×10^{-6}	5.32×10^{-6}	0	5.14×10^{-6}	4.59×10^{-6}	3.48×10^{-6}

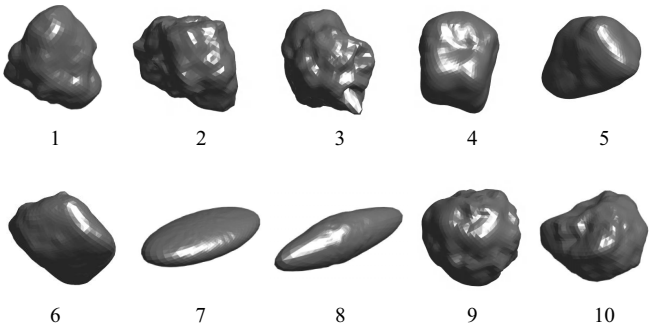

FIG. 12. Particle morphology corresponding to each ID.

where Dt_2 and Dt_1 denote two different resolutions. Considering the computational efficiency, the resolution is set to 5000 surface triangular cells. Using 0.05 as the acceptable threshold of relative error, it can be seen that the accuracy can be guaranteed when $\overline{\kappa}_c < 100$.

APPENDIX C: DISPERSION FORCE BETWEEN PARTICLES OF DIFFERENT CURVATURES WHEN $l/R = 1$

The results are given in Table III for PEC and Table IV for SiO_2.

APPENDIX D: PARTICLE MORPHOLOGY USED FOR VALIDATION

The particle morphologies corresponding to each ID in Table II are shown in Fig. 12.

[1] J. Israelachvili and B. Ninham, Intermolecular forces—the long and short of it, J. Colloid Interface Sci. **58**, 14 (1977).
[2] D. Rimai, D. Quesnel, and A. Busnaina, The adhesion of dry particles in the nanometer to micrometer-size range, Colloids Surf., A **165**, 3 (2000).
[3] A. Castellanos, The relationship between attractive interparticle forces and bulk behaviour in dry and uncharged fine powders, Adv. Phys. **54**, 263 (2005).
[4] Q. Li, V. Rudolph, and W. Peukert, London-van der Waals adhesiveness of rough particles, Powder Technol. **161**, 248 (2006).
[5] J. D. Van der Waals, *Over de Continuiteit Van Den Gas-En Vloeistoftoestand* (Sijthoff, Leiden, 1873), Vol. 1.
[6] F. London, Zur theorie und systematik der molekularkräfte, Z. Phys. **63**, 245 (1930).
[7] H. B. Casimir and D. Polder, The influence of retardation on the London-van der Waals forces, Phys. Rev. **73**, 360 (1948).
[8] E. M. Lifshitz and L. P. Pitaevskii, *Statistical Physics: Theory of the Condensed State* (Elsevier, San Diego, 2013), Vol. 9.
[9] S. Y. Buhmann, *Dispersion Forces I: Macroscopic Quantum Electrodynamics and Ground-State Casimir, Casimir–Polder and van der Waals Forces* (Springer, Heidelberg, 2013), Vol. 247.
[10] V. Svetovoy and G. Palasantzas, Influence of surface roughness on dispersion forces, Adv. Colloid Interface Sci. **216**, 1 (2015).
[11] T. Emig, A. Hanke, R. Golestanian, and M. Kardar, Probing the Strong Boundary Shape Dependence of the Casimir Force, Phys. Rev. Lett. **87**, 260402 (2001).
[12] A. W. Rodriguez, F. Capasso, and S. G. Johnson, The Casimir effect in microstructured geometries, Nat. Photonics **5**, 211 (2011).
[13] M. Wang, L. Tang, C. Ng, R. Messina, B. Guizal, J. Crosse, M. Antezza, C. T. Chan, and H. B. Chan, Strong geometry dependence of the Casimir force between interpenetrated rectangular gratings, Nat. Commun. **12**, 1 (2021).
[14] M. N. Chernodub, H. Erbin, I. Grishmanovskii, V. Goy, and A. Molochkov, Casimir effect with machine learning, Phys. Rev. Res. **2**, 033375 (2020).
[15] J. N. Israelachvili, *Intermolecular and Surface Forces* (Academic press, Waltham, 2011).
[16] M. Benz, K. J. Rosenberg, E. J. Kramer, and J. N. Israelachvili, The deformation and adhesion of randomly rough and patterned surfaces, J. Phys. Chem. B **110**, 11884 (2006).
[17] J. Dziadkowiec, S. Javadi, J. E. Bratvold, O. Nilsen, and A. Røyne, Surface forces apparatus measurements of interactions between rough and reactive calcite surfaces, Langmuir **34**, 7248 (2018).
[18] H.-J. Butt, B. Cappella, and M. Kappl, Force measurements with the atomic force microscope: Technique interpretation and applications, Surf. Sci. Rep. **59**, 1 (2005).
[19] U. Mohideen and A. Roy, Precision Measurement of the Casimir Force from 0.1 to 0.9 μm, Phys. Rev. Lett. **81**, 4549 (1998).
[20] G. Bressi, G. Carugno, R. Onofrio, and G. Ruoso, Measurement of the Casimir Force between Parallel Metallic Surfaces, Phys. Rev. Lett. **88**, 041804 (2002).
[21] J. L. Garrett, D. A. Somers, and J. N. Munday, Measurement of the Casimir Force between Two Spheres, Phys. Rev. Lett. **120**, 040401 (2018).
[22] H. R. Moutinho, C.-S. Jiang, B. To, C. Perkins, M. Muller, M. M. Al-Jassim, and L. Simpson, Adhesion mechanisms on solar glass: Effects of relative humidity surface roughness, and particle shape and size, Sol. Energy Mater. Sol. Cells **172**, 145 (2017).
[23] P. Zhao and Y. Li, Correlation between the normal position of a particle on a rough surface and the van der Waals force, Colloids Surf., A **585**, 124096 (2020).
[24] C. A. Stevenson, J. E. Monroe, C. G. Norris, A. R. Roginski, and S. P. Beaudoin, The effects of surface and particle properties on van der Waals (vdW) adhesion quantified by the enhanced centrifuge method, Powder Technol. **392**, 514 (2021).
[25] Y. Nagaashi, T. Aoki, and A. M. Nakamura, Cohesion of regolith: Measurements of meteorite powders, Icarus **360**, 114357 (2021).
[26] L. Tang, M. Wang, C. Ng, M. Nikolic, C. T. Chan, A. W. Rodriguez, and H. B. Chan, Measurement of non-monotonic casimir forces between silicon nanostructures, Nat. Photonics **11**, 97 (2017).

[27] M. Sedighi, V. Svetovoy, and G. Palasantzas, Casimir force measurements from silicon carbide surfaces, Phys. Rev. B **93**, 085434 (2016).
[28] V. Svetovoy, A. Postnikov, I. Uvarov, F. Stepanov, and G. Palasantzas, Measuring the Dispersion Forces Near the van der Waals–Casimir Transition, Phys. Rev. Appl. **13**, 064057 (2020).
[29] I. Soldatenkov, F. Stepanov, and V. Svetovoy, Dispersion forces and equilibrium distance between deposited rough films in contact, Phys. Rev. B **105**, 075401 (2022).
[30] V. A. Parsegian, *Van der Waals Forces: A Handbook for Biologists, Chemists, Engineers, and Physicists* (Cambridge University Press, New York, 2005).
[31] J.-P. Sonnenberg and E. Schmidt, Numerical calculation of London-van der Waals adhesion force distributions for different superquadric shaped particles, Part. Part. Syst. Charact. **22**, 45 (2005).
[32] J. C. Hopkins, R. Podgornik, W.-Y. Ching, R. H. French, and V. A. Parsegian, Disentangling the effects of shape and dielectric response in van der Waals interactions between anisotropic bodies, J. Phys. Chem. C **119**, 19083 (2015).
[33] H. C. Hamaker, The London-van der Waals attraction between spherical particles, Physica **4**, 1058 (1937).
[34] I. E. Dzyaloshinskii, E. M. Lifshitz, and L. P. Pitaevskii, The general theory of van der Waals forces, Adv. Phys. **10**, 165 (1961).
[35] H. Gies and K. Klingmüller, Casimir Effect for Curved Geometries: Proximity-Force-Approximation Validity Limits, Phys. Rev. Lett. **96**, 220401 (2006).
[36] A.-F. Bitbol, A. Canaguier-Durand, A. Lambrecht, and S. Reynaud, Pairwise summation approximation for Casimir potentials and its limitations, Phys. Rev. B **87**, 045413 (2013).
[37] P. S. Venkataram, J. D. Whitton, and A. W. Rodriguez, Nonadditivity of van der Waals forces on liquid surfaces, Phys. Rev. E **94**, 030801 (2016).
[38] P. S. Venkataram, J. Hermann, A. Tkatchenko, and A. W. Rodriguez, Unifying Microscopic and Continuum Treatments of van der Waals and Casimir Interactions, Phys. Rev. Lett. **118**, 266802 (2017).
[39] T. Emig, N. Graham, R. Jaffe, and M. Kardar, Casimir Forces between Arbitrary Compact Objects, Phys. Rev. Lett. **99**, 170403 (2007).
[40] M. H. Reid, J. White, and S. G. Johnson, Fluctuating surface currents: An algorithm for efficient prediction of Casimir interactions among arbitrary materials in arbitrary geometries, Phys. Rev. A **88**, 022514 (2013).
[41] T. Emig, N. Graham, R. Jaffe, and M. Kardar, Orientation dependence of Casimir forces, Phys. Rev. A **79**, 054901 (2009).
[42] M. Chernodub, V. Goy, and A. Molochkov, Casimir effect on the lattice: $U(1)$ gauge theory in two spatial dimensions, Phys. Rev. D **94**, 094504 (2016).
[43] A. Rodriguez, M. Ibanescu, D. Iannuzzi, J. Joannopoulos, and S. G. Johnson, Virtual photons in imaginary time: Computing exact Casimir forces via standard numerical electromagnetism techniques, Phys. Rev. A **76**, 032106 (2007).
[44] A. W. Rodriguez, A. P. McCauley, J. D. Joannopoulos, and S. G. Johnson, Casimir forces in the time domain: Theory, Phys. Rev. A **80**, 012115 (2009).
[45] S. G. Johnson, in *Casimir Physics* (Springer, Heidelberg, 2011), p. 175.
[46] M. H. Reid, A. W. Rodriguez, J. White, and S. G. Johnson, Efficient Computation of Casimir Interactions between Arbitrary 3D Objects, Phys. Rev. Lett. **103**, 040401 (2009).
[47] Z.-K. Feng, W.-J. Xu, and R. Lubbe, Three-dimensional morphological characteristics of particles in nature and its application for dem simulation, Powder Technol. **364**, 635 (2020).
[48] V. Angelidakis, S. Nadimi, and S. Utili, Shape analyser for particle engineering (shape): Seamless characterisation and simplification of particle morphology from imaging data, Comput. Phys. Commun. **265**, 107983 (2021).
[49] ISO, Representation of results of particle size analysis—Part 6: Descriptive and quantitative representation of particle shape and morphology, ISO 9276-6:2008 ed. (International Organization for Standardization, Vernier, Geneva, Switzerland, 2008).
[50] T. Kämäräinen, M. Ago, J. Seitsonen, J. Raula, E. I. Kauppinen, J. Ruokolainen, and O. J. Rojas, Harmonic analysis of surface instability patterns on colloidal particles, Soft Matter **14**, 3387 (2018).
[51] H. Wadell, Volume, shape, and roundness of rock particles, J. Geol. **40**, 443 (1932).
[52] D. W. Luerkens, J. K. Beddow, and A. Vetter, Morphological Fourier descriptors, Powder Technol. **31**, 209 (1982).
[53] B. Zhao and J. Wang, 3D quantitative shape analysis on form roundness, and compactness with μCT, Powder Technol. **291**, 262 (2016).
[54] N. Fauchereau, G. Pegram, and S. Sinclair, Empirical mode decomposition on the sphere: Application to the spatial scales of surface temperature variations, Hydrol. Earth Syst. Sci. **12**, 933 (2008).
[55] N. Rehman and D. P. Mandic, Multivariate empirical mode decomposition, Proc. R. Soc. A **466**, 1291 (2010).
[56] N. E. Huang, Z. Shen, S. R. Long, M. C. Wu, H. H. Shih, Q. Zheng, N.-C. Yen, C. C. Tung, and H. H. Liu, The empirical mode decomposition and the Hilbert spectrum for nonlinear and non-stationary time series analysis, Proc. R. Soc. A **454**, 903 (1998).
[57] Y. Liu, D.-S. Jeng, H. Xie, and C. Li, On the particle morphology characterization of granular geomaterials, Acta Geotech. **8**, 1 (2022).
[58] https://github.com/yfliu088/GMAP.
[59] J. Zheng and R. D. Hryciw, Traditional soil particle sphericity roundness and surface roughness by computational geometry, Géotechnique **65**, 494 (2015).
[60] B. Zhou, J. Wang, and H. Wang, Three-dimensional sphericity roundness and fractal dimension of sand particles, Géotechnique **68**, 18 (2018).
[61] G. E. Schröder-Turk, W. Mickel, S. C. Kapfer, F. M. Schaller, B. Breidenbach, D. Hug, and K. Mecke, Minkowski tensors of anisotropic spatial structure, New J. Phys. **15**, 083028 (2013).
[62] M. H. Reid, Ph.D. thesis, Massachusetts Institute of Technology (2011).

[63] M. H. Reid and S. G. Johnson, Efficient computation of power force, and torque in bem scattering calculations, IEEE Trans. Antennas Propag. **63**, 3588 (2015).
[64] S. Rao, D. Wilton, and A. Glisson, Electromagnetic scattering by surfaces of arbitrary shape, IEEE Trans. Antennas. Propag. **30**, 409 (1982).
[65] M. Moazzami Gudarzi and S. H. Aboutalebi, Self-consistent dielectric functions of materials: Toward accurate computation of Casimir–van der Waals forces, Sci. Adv. **7**, eabg2272 (2021).
[66] D. Wei, J. Wang, and B. Zhao, A simple method for particle shape generation with spherical harmonics, Powder Technol. **330**, 284 (2018).
[67] E. M. Lifshitz and M. Hamermesh, in *Perspectives in Theoretical Physics* (Pergamon Press, Oxford, 1992), p. 329.
[68] https://github.com/yfliu088/vdw-casimir.
[69] P. M. Neto, A. Lambrecht, and S. Reynaud, Roughness correction to the Casimir force: Beyond the proximity force approximation, EPL **69**, 924 (2005).
[70] D. Krause, R. Decca, D. López, and E. Fischbach, Experimental Investigation of the Casimir Force Beyond the Proximity-Force Approximation, Phys. Rev. Lett. **98**, 050403 (2007).
[71] M. Hartmann, G.-L. Ingold, and P. A. M. Neto, Plasma versus Drude Modeling of the Casimir Force: Beyond the Proximity Force Approximation, Phys. Rev. Lett. **119**, 043901 (2017).
[72] G. Bimonte, Beyond-proximity-force-approximation Casimir force between two spheres at finite temperature, Phys. Rev. D **97**, 085011 (2018).
[73] S. Eichenlaub, A. Gelb, and S. Beaudoin, Roughness models for particle adhesion, J. Colloid Interface Sci. **280**, 289 (2004).
[74] C. Q. LaMarche, S. Leadley, P. Liu, K. M. Kellogg, and C. M. Hrenya, Method of quantifying surface roughness for accurate adhesive force predictions, Chem. Eng. Sci. **158**, 140 (2017).
[75] M. Bordag, G. Klimchitskaya, and V. Mostepanenko, Corrections to the Casimir force between plates with stochastic surfaces, Phys. Lett. A **200**, 95 (1995).